This paper is the accepted version of the paper published on IEEE Transactions On Geoscience And Remote Sensing, Vol. 56, No. 10, October 2018

Digital Object Identifier 10.1109/TGRS.2018.2828604

The Ultra-Wideband Software Defined Microwave Radiometer: Instrument Description and Initial Campaign Results

Mark Andrews, Joel T. Johnson, Kenneth C. Jezek[1], Hongkun Li, Alexandra Bringer, Chi-Chih Chen, Domenic Belgiovane, Vladimir Leuski[3], Giovanni Macelloni[2], Marco Brogioni[2]
ElectroScience Laboratory, The Ohio State University, Columbus, OH
[1]Byrd Polar Research Center, The Ohio State University, Columbus, OH
[2]Institute of Applied Physics, Florence, Italy
[3]Microwave Radiometers and Antennas, Louisville, CO

***Abstract*— The Ultra-Wideband Software Defined Microwave Radiometer (UWBRAD) is a 500-2000 MHz radiometer developed to probe temperatures inside ice sheets. Given the instrument's operation outside of protected portions of the spectrum, radio frequency interference (RFI) is a significant concern, and the instrument is designed to facilitate RFI detection and filtering. This document analyzes the design and operation of the radiometer, the accuracy and stability of the brightness temperatures it produces, and RFI analyses of the results acquired in its debut flight over northern Canada and Greenland in September 2016.**

***Index Terms*—radiometry, microwave radiometry, UHF radiometry, calibration, ultrawideband radiation, electromagnetic interference, remote sensing**

I. Introduction

At present, several geophysical properties that characterize the dynamics of the polar ice sheets cannot be derived remotely and are derived only by ground measurements or glaciological models. Ice sheet internal temperature is one of these properties. The only measured information at present is obtained from a small number of deep ice core sites. Previous studies [1]-[7] have demonstrated the potential of multi-frequency brightness temperature measurements from 500-2000 MHz to obtain internal ice sheet temperature information. The Ultra-Wideband Software Defined Microwave Radiometer (UWBRAD) was funded through NASA's Instrument Incubator Program to provide a demonstration of these new concepts and to investigate the use of 500-2000 MHz more generally. Because the frequency range 500-2000 MHz is a crowded portion of the spectrum with only a small portion of the range protected for scientific use, UWBRAD is required to operate in the presence of significant radio frequency interference (RFI). There are three main objectives for UWBRAD: 1) to observe ice sheet brightness temperatures in the frequency range of 500-2000 MHz, 2) to identify and mitigate any radio frequency interference (RFI) through software defined algorithms in real-time and in post-processing, and 3) to determine internal sub-surface ice sheet temperatures through model based retrieval algorithms using measured brightness temperatures.

This article presents the design of the UWBRAD instrument (Section II), a description of how calibration is performed and the results of calibration testing on the instrument (Section III and IV), a description of the RFI algorithms used (Section V), and the initial results (brightness temperatures and RFI statistics) of an airborne campaign conducted in Greenland in September 2016 (Section VI). Additional information on ice sheet physical property measurements using UWBRAD is provided in a companion paper [8].

II. Description

The UWBRAD system is composed of an ultra-wide bandwidth conical spiral antenna (Section A), a radio frequency (RF) frontend (Section B), intermediate frequency (IF) downconversion units (Section C), and an analog-to-digital (A/D) conversion backend and data processor (Section D). UWBRAD also includes heaters for thermal control of the RF frontend and IF units. A high level block diagram and photo of the system is presented in Fig. 1.

A. Antenna

The antenna [9] is a conical log spiral design including an internal balun feed (Fig. 2 left), conical antenna elements (Fig. 2 center), and a protective radome (Fig. 2 right). The antenna

This manuscript was submitted for review on December 1, 2017. This work was supported by NASA's Earth Science Technology Office's Instrument Incubator Program, under Grant NNX14AE68G and in part by NASA's Cryospheric Sciences Program under Grant NNX14AH91G.

M. J. Andrews, J. T. Johnson, C.-C. Chen, D. J. Belgiovane, Jr., H. Li, and A. Bringer are with the ElectroScience Laboratory, The Ohio State University, Columbus, OH 43212 USA (e-mail: andrews.250@osu.edu).

K. C. Jezek, is with the Byrd Polar and Climate Research Center, School of Earth Sciences, The Ohio State University, Columbus, OH 43210 USA.

M. Brogioni and G. Macelloni are with the Institute of Applied Physics "Nello Carrara," National Research Council, 50019 Florence, Italy.

V. Leuski is with Microwave Radiometer and Antennas, LLC, University of Colorado Boulder, Boulder, CO 80027 USA.

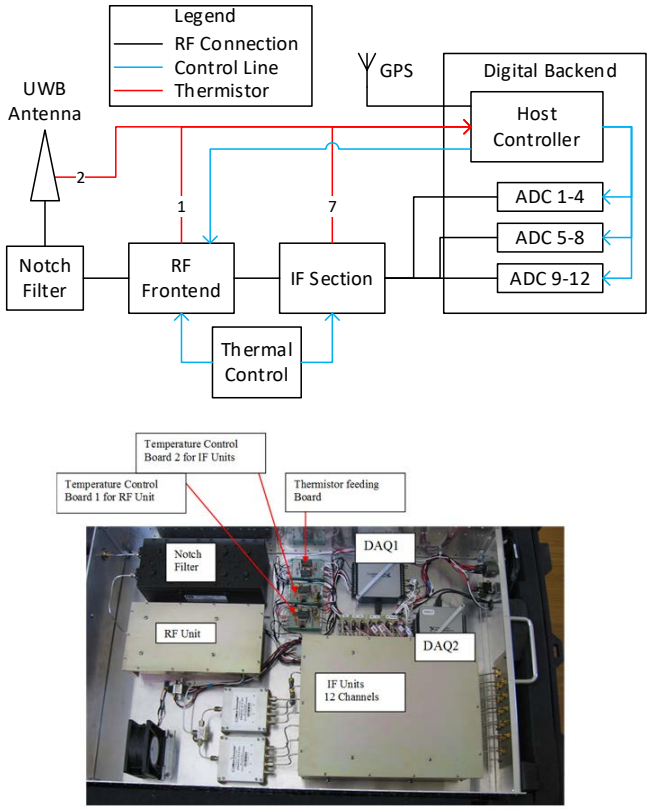

Fig. 1: Top: block diagram of UWBRAD system. The numbers on the red thermistor lines indicate how many thermistors are located in the corresponding subsystems. Bottom: Photo of UWBRAD system from notch filter through IF units

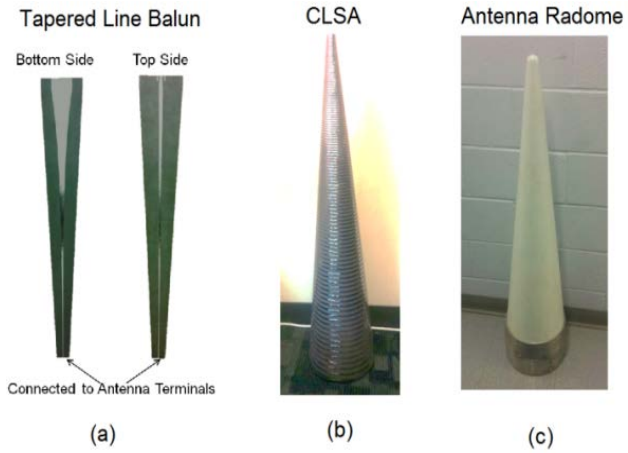

Fig. 2: Images of a) internal balun board, b) conical log spiral antenna, and c) radome over antenna

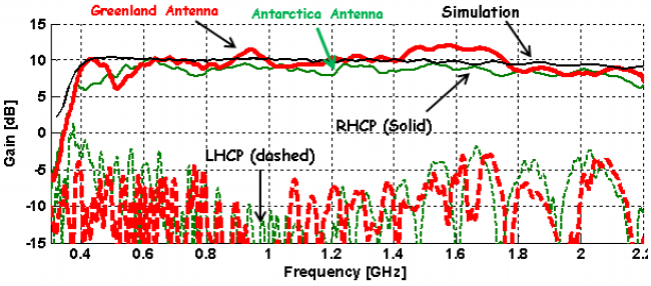

Fig. 3: Measured and simulated UWBRAD antenna gains (red lines for Greenland campaign)

provides near constant gain (and footprint size for a specific platform altitude) from 500-2000 MHz. The antenna is deployed out of the bottom of the aircraft using a "periscope" system and is oriented to nadir when the aircraft is in level flight. Two antennas were created: one for use on an engineering model that was tested at DOME-C (Antarctica Antenna), and one for use in flight (Greenland Antenna). The antenna design was simulated using the aircraft frame and measurements were taken in an anechoic chamber. Fig. 3 plots the simulated and measured values of the gains of both of these antennas, and shows gain for the antenna used in Greenland of approximately 10 dB across the frequencies of interest (with a corresponding ~60 degree half-power beamwidth) for right hand circular polarization (RHCP). RHCP was chosen as it simplified the ultra-wideband antenna design and met the model requirements for determining internal ice sheet temperatures. For an aircraft operating at the nominal altitude of 500 m, the resulting circular footprint is ~0.6 km in diameter, requiring approximately 7.5 seconds to traverse at the nominal flight speed of 150 kts. Radome losses for the antenna ranged from 0 to 0.5 dB, and balun losses ranged from 0.1 to 0.4 dB. Measured total losses for the antenna from the campaign (including radome, balun, mismatch, and cable losses) ranged from 1 to 4 dB, with 2.5 to 3.5 dB being typical. Reference [9] contains additional details regarding the antenna design.

B. RF Frontend

A typical Dicke radiometer design was considered for UWBRAD, but finding components (e.g., ferromagnetic isolators) that provide high isolation (>20 dB) and low loss (<1dB) over the desired bandwidth proved challenging, and splitting the signal to more manageable bandwidths would create additional losses and complexity that was undesirable. Wide bandwidth 90° hybrid couplers (hybrids) are available (Werlatone QH7900) that better met the project's isolation and loss requirements (>18 dB and <0.55 dB, respectively), so a pseudo-correlation radiometer design was pursued, as shown in Fig. 4. In typical implementations of this design, two outputs (one approximately representing a reference load and the other the antenna) are observed simultaneously to determine continuously the real-time parameters of the system and derive the observed brightness temperature. For UWBRAD, measurement of both outputs simultaneously was undesirable (doubling the IF and digital subsystems), so UWBRAD measures the two output signals sequentially (by toggling a phase shifter) to perform internal calibration.

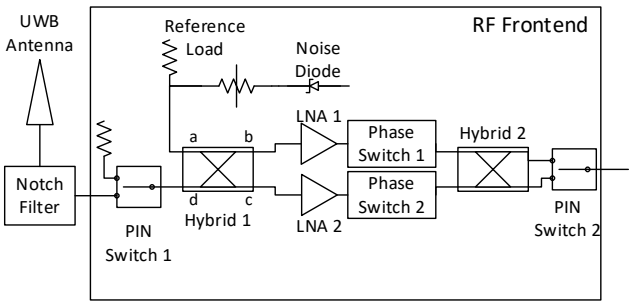

Fig. 4: Block diagram of UWBRAD RF frontend pseudo-correlation design

The RF frontend unit has two inputs to the first 90° quadrature hybrid: the antenna port (labeled 'd') and the reference port (labeled 'a'). The reference inputs include a 50 ohm termination at a known physical temperature combined with a switchable noise diode of known apparent temperature to allow a two point calibration. The antenna port has a switch (PIN Switch 1) that can be used to view a 50 ohm termination instead of the antenna to reduce potential interference when viewing the reference port. These signals then pass through the hybrid to two matched amplifier chains, each with an electronic 0°/180° phase shifter (Phase Switch 1 and 2). A second 90° hybrid is located at the output, with another switch (PIN Switch 2) used to select which output of the second hybrid to measure and which to terminate in 50 ohms.

In the UWBRAD frontend, the four switches identified plus the noise diode give the possibility of 32 (2^5) states of the radiometer available to be observed. The noise diode and PIN Switch 1 define the two inputs into the system: antenna plus reference, antenna plus noise diode, antenna terminated plus reference, and antenna terminated plus noise diode. Due to imbalances in the gain and phase of the two paths, the outputs of the second hybrid have a dominant and minor term associated with each of the inputs (explored further in Section III): one output is reference dominant/antenna minor and the other is antenna dominant/reference minor. The remaining three switches all have the effect of toggling which output is being viewed. The phase shifters do so by changing the electrical phase of one path by 180°, changing the interference pattern such that what was destructive interference becomes constructive and vice versa. PIN Switch 2 does so by observing the other output of the second hybrid. Activating two of these switches at the same time simply toggles twice, leaving the original signal. During calibration testing, no clear benefit emerged for using any particular combination of these three switches, so Phase Switch 1 was chosen to toggle between the outputs, and Phase Switch 2 and PIN Switch 2 were not switched in the calibration process.

C. IF Downconversion Units

After the RF frontend, the amplified radiometer signal is divided into ten ~81 MHz bandwidth channels and two ~60 MHz channels as shown in Fig. 5. This channel configuration was chosen based on the sampling rate of the A/D cards and digital backend processing rate. Keeping the channels as large as possible minimizes the hardware cost and complexity, while allowing the option of integrating the data to smaller bandwidth subchannels in post-processing (at the cost of increasing the measurement uncertainty of each subchannel) to best fit the needs of any given ice sheet temperature prediction model. Bandpass filters (Fig. 6) are used on each channel to help prevent out-of-band interference from affecting all channels. A thirteenth channel was originally planned, but was removed due to a powerful transmitter on the aircraft around 1000 MHz, which the notch filter identified in Fig. 4 helps mitigate. Seven local oscillators (LO) are used to downconvert the twelve channels to a common 180 MHz IF frequency for A/D conversion by the digital backend (operating in the first Nyquist zone of the A/D cards). Ten of the twelve channels are paired in an upper and lower sideband configuration with a common LO. The smaller gap around 750 MHz visible in Fig. 6 is a result of keeping channel 5 (1170 MHz) away from the rejection region of the notch filter and sharing an LO with channel 3 (810 MHz). The remaining two channels have a dedicated LO. After downconversion, each channel has an antialiasing bandpass filter before being sent on to the digital backend.

D. Analog-to-Digital Backend and Software

The digital backend is composed of four computers: one host computer and three A/D conversion clients. The host

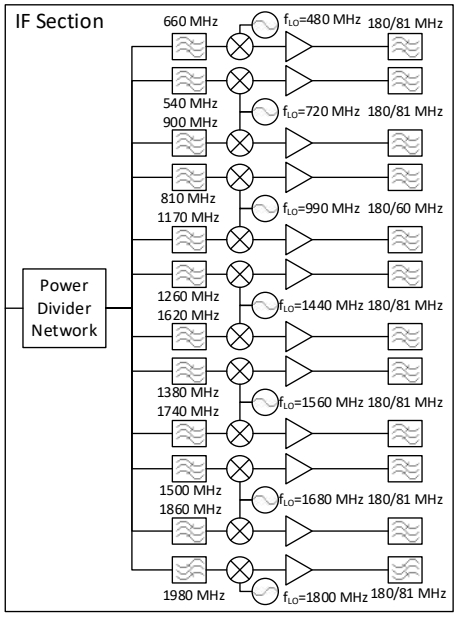

Fig. 5: Block diagram of UWBRAD IF section

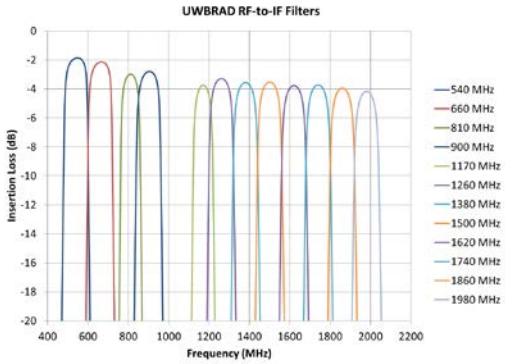

Fig. 6: Specified channel filter responses in IF section

computer is responsible for acquiring ancillary data (such as temperature and GPS information) and triggers acquisition of data on the three client computers. The client computers wait for a signal from the host to acquire data, then process and store the data. The client computers each hold two AlazarTech A/D conversion cards that convert two channels per card. These cards operate at 250 MS/s at 16 bits per sample. Once the signal has been sampled digitally, fast Fourier transforms (FFTs) and RFI processing are done in software before saving data products to hard disk. Performing these tasks in software enables updates to RFI algorithms, flagging thresholds, acquisition time and data processing for future (or changing) mission requirements. The client computers each hold eight 4 TB hard drives for data storage. Each channel has a dedicated hard drive with automatic backup to a second drive (RAID 1 configuration).

Each acquisition performed by the digital backend is 100 ms long. Storing all of the raw samples would require an excessive amount of storage space, so in normal operations the raw data is processed into "medium rate" and "low rate" data for storage. Medium rate data stores time domain power in 100 x 1 ms intervals, and also uses Fast Fourier Transforms (FFT) to create a 512 bin spectrogram for each 1 ms interval, resulting in a 512 x 100 point spectrogram matrix in the medium rate data product. The kurtosis of each 1 ms interval as well as the subband kurtosis of each frequency bin are calculated and also stored in medium rate files. The first four moments are calculated to determine kurtosis, and all FFT and kurtosis information is stored in floating point double format. RFI algorithms are run onboard (fullband kurtosis, pulse blanking, subband kurtosis, cross frequency) and the flags for each algorithm are stored to complete the medium rate data product. The low rate data product integrates over the entire channel before and after RFI algorithms are applied and stores these two numbers as well as the total percentage of data flagged as RFI. The low rate data product was recorded as a proof of concept for future missions with more restrictive data requirements (e.g., spaceborne radiometry), but the UWBRAD team currently only uses the more detailed medium rate product for its analyses.

It is necessary to acquire four different states (400 ms of data, 100 ms of which is considered "antenna" data) to achieve a calibrated brightness temperature (details in section III). The time required to acquire, process, and store these states averages around 2 seconds, so that the final duty cycle of UWBRAD antenna measurements is approximately 5%. This is not a problem for UWBRAD as ample integration time is available per footprint, and it is assumed that the antenna temperature is constant during acquisition of the four states due to the large footprint. It would be possible to increase the duty cycle by performing extra antenna measurements between internal calibration state measurements, but this has not been pursued at this time.

III. CALIBRATION

To determine a calibration procedure for the radiometer, a mathematical formulation for the signals present at the output of the RF unit is needed. A summary of the voltage signals of interest for the derivation is provided in Table I. Using these variables, the complex voltages of the front end can be summarized in the form of equations (1) and (2).

$$V^0 = V_R\left(H_{1,ca}G_2H_{2,cd} + H_{1,ba}G_1H_{2,ca}\right) + V_A\left(H_{1,cd}G_2H_{2,cd} + H_{1,bd}G_1H_{2,ca}\right) + V_{N1}G_1H_{2,ca} + V_{N2}G_2H_{2,cd} \quad (1)$$

$$V^{180} = V_R\left(H_{1,ca}G_2H_{2,cd} - H_{1,ba}G_1H_{2,ca}\right) + V_A\left(H_{1,cd}G_2H_{2,cd} - H_{1,bd}G_1H_{2,ca}\right) + V_{N1}G_1H_{2,ca} + V_{N2}G_2H_{2,cd} \quad (2)$$

In equations (1) and (2), the phases of the H terms constructively and destructively interfere such that V^0 will have a large gain term (approximately 2G where G is the gain of one amplifier) for V_R and a term near 0 for V_A. When the phase switch is in the 180° position, the interference pattern alternates such that V_R will now have a small gain and V_A will have the large gain. Ideally, the gain and phase of the two paths would be identical, eliminating the minor term in the measurements. Achieving this over all frequency and all environmental conditions is exceedingly difficult, so a calibration scheme that accounts for the minor term is needed.

Table I: Voltage Variables

V^X	Output voltage when Phase Switch 1 is in X degree position
V_A	Voltage at the antenna input port of the radiometer
V_R	Voltage of the reference load input port of the radiometer
G_1	Voltage gain (magnitude only) of LNA path 1
G_2	Voltage gain (magnitude only) of LNA path 2
V_{N1}	Added noise voltage from active circuits in path 1
V_{N2}	Added noise voltage from active circuits in path 2
$H_{x,zy}$	Transmission coefficient of hybrid X from port y to port z. Includes 90 degree phase shift for bd and ca paths, 0 degrees for cd and ba

Calculating the power of the outputs (computing the amplitude squared of the signal) causes cross products of the various terms to appear. Since these are all independent random noise signals, integrating over time will cause these cross products to vanish, leaving the following equations to describe the system (variables defined in Table II):

$$P^0 = C_R^0T_R + C_A^0T_A + N \quad (3)$$

$$P^{180} = C_R^{180}T_R + C_A^{180}T_A + N \quad (4)$$

Table II: Power Variables

P^X	Output power when Phase Switch 1 is in X degree position
$C_{R/A}^X$	Gain coefficient (W/K) for reference (R) or antenna (A) path when Phase Switch 1 is at X degrees.
$T_{R/A}$	Noise temperature of reference (R) or antenna (A) input port
N	Added noise power in system due to active circuits

The net result is that the output has a dominant term proportional to one input signal, a smaller term proportional to the other input signal, and an offset from the noise added due to active circuits (LNA and phase shifter). Toggling a phase switch was chosen instead of using PIN Switch 2 so that the added noise in the system followed the same path through the output hybrid. Assuming the phase shifter's added noise component remains constant with its setting, this would result in the same N term for all measurements. Lab tests showed that using Phase Switch 2 or PIN Switch 2 instead is similarly effective, so the "0" and "180" states can be used with any switch or combination of switches without losing generality.

There are now four radiometer states that can be observed: dominant reference signal with noise diode on/off, and dominant antenna signal with noise diode on/off. Using these states, the calibration sequence to determine the temperature at the antenna input port is:

1. Measure both phase switch positions with the noise diode off, then subtract the results (A):
$$(C_R^0 T_R + C_A^0 T_A + N) - (C_R^{180} T_R + C_A^{180} T_A + N) = (C_R^0 - C_R^{180})T_R + (C_A^0 - C_A^{180})T_A$$

2. Measure both phase switch positions with the noise diode on, then subtract the results (B):
$$(C_R^0[T_R + T_D] + C_A^0 T_A + N) - (C_R^{180}[T_R + T_D] + C_A^{180} T_A + N) = (C_R^0 - C_R^{180})[T_R + T_D] + (C_A^0 - C_A^{180})T_A$$

3. Subtract (A) from (B) to obtain
$$(C_R^0 - C_R^{180})T_D$$

4. Define
$$Q = \frac{A}{B - A} = \frac{T_R}{T_D} + \frac{T_A}{T_D} f$$
where
$$f = \frac{(C_A^0 - C_A^{180})}{(C_R^0 - C_R^{180})}$$

With T_R(reference load physical temperature measured by a thermistor), T_D(excess temperature due to the noise diode, derived through lab testing), and f (derived through lab testing) defined, T_A can be solved for from the four state measurements. The final calibration sequence acquires and processes 100 ms of each of these four states (antenna/noise diode off and antenna /noise diode on with phase switch in both positions) repeatedly and calculates a single brightness temperature from each set of four measurements. This process assumes that T_D and f are stable parameters once calibrated, and it was found that modeling these parameters as constants resulted in a stable calibration of UWBRAD over temperature. Additional averaging of measurements, particularly the B - A term in the denominator of the Q parameter (which is independent of antenna input signal), is possible to further improve the accuracy and stability of the system, and adding additional antenna dominant measurements to the calibration sequence may be able to increase the duty cycle of brightness temperature retrieval. Both of these approaches are still under further study for UWBRAD and have yet to be implemented.

IV. Lab Results

Laboratory testing was used to determine the excess brightness of the noise diode (T_D) and the gain ratio parameter f. A digital step attenuator was attached to the radiometer input and connected to a cable terminated in a matched 50 ohm load, which was placed in liquid nitrogen (LN2). The temperature of the room and the S-parameters of the cable and step attenuator were measured to determine the truth input temperature at the radiometer input for each attenuator value. The entire system was placed in a thermal chamber and the attenuators cycled through their values while the chamber temperature ranged from 0 to 30 °C. This temperature range was chosen to cover the expected conditions in the airplane during flight. The test was performed for a continuous 24 hour period to derive the calibration of the radiometer. Repeated liquid nitrogen tests performed at ambient temperatures before the campaign showed similar results, suggesting a stable noise diode and system performance.

The Q parameter was calculated from the various state powers recorded and line fit versus the known input temperature for each frequency bin to determine the noise diode temperature and f parameter. The results versus frequency are shown in Fig. 7. These results appear to exhibit an anti-correlation, which may or may not be real as the slope (f/T_D) and the offset (T_R/T_D) are related by T_D. However, all of the results contained in this paper use the parameters as shown.

Each channel is processing 125 MHz of observable bandwidth. However, the IF filters and anti-alias filters are designed to be narrower than the available bandwidth to provide isolation from out-of-band effects, and the filters also are not perfectly centered or symmetrical with the observed bandwidth. As a result, the gain at some band edges eventually reduces to the point that the ADC does not have the precision to retrieve antenna temperatures accurately. Once the root mean square error (RMSE) of a frequency bin exceeds a certain threshold, these band edges are removed from the calculation to reduce the RMSE of the retrieved temperatures. After performing RFI processing and integrating over frequency for each of the 12 channels, the RMSE from the predicted input temperature for the channels ranged from 0.28-0.48 K for a 100 ms integration period, detailed in the third column of Table III, and followed by the resulting system temperature determined from this value. The second column shows the average bandwidth of the channel during LN2 testing after removal of band edges and RFI processing (some internal spurious signals can be detected and flagged, reducing the bandwidth). The goal was an error of 1 K for each channel, so these laboratory tests confirm that the radiometer met the desired performance for all 12 channels. Fig. 8 shows a spectrogram example of one channel (channel 7, 1380 MHz center frequency, 512 frequency bins) and the error between the retrieved temperature and predicted input temperature. The degradation of the band edges can be seen below 1320 MHz and above 1430 MHz, and some small internal interference can be seen around 1335 and 1395 MHz. These bins are either removed manually (in the case of band edges) or by RFI flagging (for interferers) before calculating final temperatures.

Table III: UWBRAD channel performance

Channel	Center Frequency (MHz)	Average Bandwidth (MHz)	RMSE (K)	T_{sys} (K)[2]
1	540	86	0.33	684
2	660	90	0.34	764
3	810	75[1]	0.48	665
4	900	102	0.35	784
5	1170	78[1]	0.31	652
6	1260	105	0.29	679
7	1380	104	0.34	817
8	1500	108	0.28	701
9	1620	106	0.33	758
10	1740	98	0.31	646
11	1860	102	0.35	884
12	1980	83	0.44	1013

[1]IF filter designed for a minimum 3-dB bandwidth of 60 MHz. All other channels designed for 81 MHz minimum bandwidth.
[2]System temperature is averaged over all liquid nitrogen testing and calculated as $T_{sys} = RMSE * \sqrt{B * \tau} - T_{in}$, where *RMSE* is the error of the channel, B is bandwidth, τ is integration time, and T_{in} is input temperature

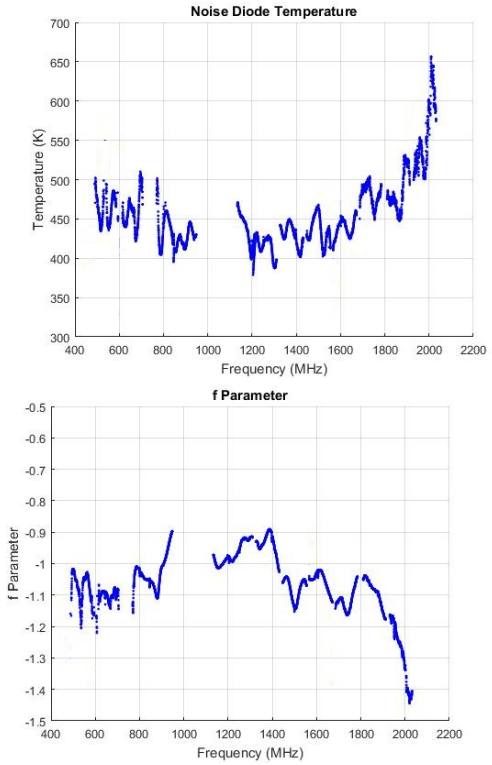

Fig. 7: Calibration results for noise diode temperature (top) and f gain ratio parameter (bottom)

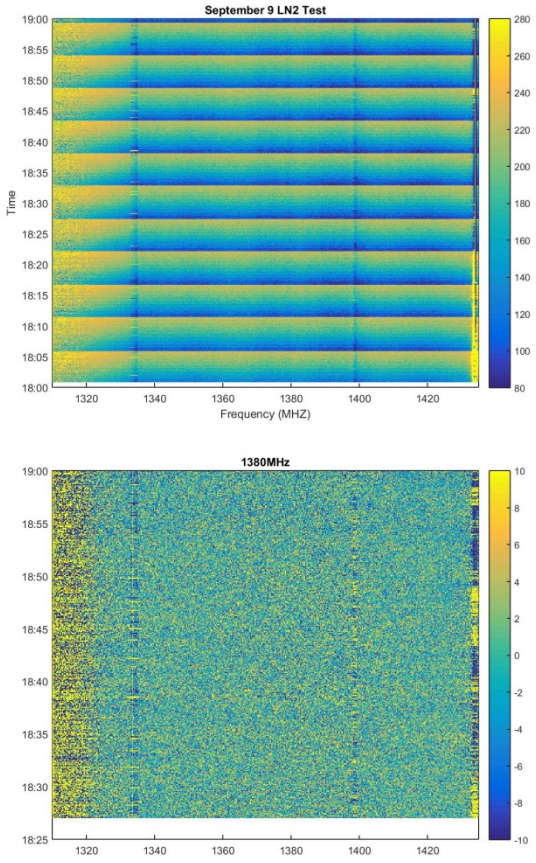

Fig. 8: LN2 test retrieval spectrogram for 1380 MHz channel as the input brightness temperatures are cycled over a range of values in periodic fashion (top) and difference between calibrated and known input temperatures (bottom)

V. RFI Algorithms

Given UWBRAD's wide bandwidth operation in unprotected bands, many types of RFI were expected to be encountered. RFI detection algorithms working in the time, frequency and statistics domains were therefore used for UWBRAD, following a process similar to that used for the SMAP microwave radiometer [10]. As with SMAP, UWBRAD produces both "fullband" (i.e. time domain powers representing the entire bandwidth in a given channel) and "sub-band" (spectrograms of the integrated power in 512 frequency channels at 1 ms time resolution) products. UWBRAD applies its time domain algorithms first (Level 1 Processing) using fullband products to flag short pulsed and non-Gaussian RFI. Then sub-band algorithms are applied (Level 2 Processing) to flag any frequency dependent RFI.

In Level 1 Processing, each 100 ms acquisition is divided into 100 x 1 ms intervals, and the kurtosis and integrated power for each of these intervals are computed. The fullband kurtosis algorithm is applied first and operates on-board in real-time. The fullband kurtosis algorithm flags any 1 ms intervals having a kurtosis value outside a user defined range (2.86-3.14 for this campaign) as RFI. As the kurtosis algorithm is the first applied, the threshold is deliberately kept loose (near zero false alarm rate) so as not to excessively discard data that may be flagged more precisely by later algorithms (such as continuous wave or pulsed interference).

The pulse blanking algorithm also operates in real time, but was recomputed for this campaign in post-processing in order to optimize performance. The algorithm used is based on the Median Absolute Deviation method [11] and operates on the 512 x 100 point spectrogram of the received power. After fullband kurtosis flagged intervals are discarded, the pulse blanking algorithm calculates the median value of the power in the remaining 1 ms intervals for each frequency bin. The median value of each bin is subtracted from the spectrogram, resulting in a signal centered near zero for most samples. The median of the absolute value of this deviation is then calculated. Any time intervals for which the power deviation exceeds 4 times the median absolute deviation are then flagged as pulses. This results in a false alarm rate (FAR) of approximately 1% for each frequency bin. The final Level 1 product is created by integrating the UWBRAD spectrogram over the 100 ms measurement interval both including (unmitigated) and excluding (mitigated) 1 ms intervals flagged by the kurtosis and pulse blanking algorithms, representing power in 512 frequency bins at 100 ms time resolution.

Fig. 10 (in Section VI) shows the spectrograms of observed brightness temperatures during the transit flight of the campaign before and after each stage of RFI processing. The middle spectrogram in each figure shows the Level 1 product for the scenes after application of the fullband kurtosis and pulse detection algorithms. Several examples of pulsed RFI are removed, and in some cases, entire channels are flagged as RFI (particularly early on, near population centers Calgary and Edmonton).

The processing to Level 1 operates directly on the recorded powers. At this point, the data is calibrated using the procedures described in Section III to obtain antenna temperatures resolved into 512 frequency bins (over the full measured 125 MHz frequency range including band edges) at 100 ms time resolution. These antenna temperatures are then converted to scene temperatures using measurements over water bodies during the campaign for external calibration. The cross frequency algorithm is now applied for each 100 ms interval to identify anomalous frequency bins. The cross frequency algorithm is similar to the algorithm presented in Guner [12]. However, rather than using the mean of the lowest 85% of antenna temperatures in setting detection thresholds, it uses the median value across frequency of the antenna temperature instead. Thresholds for this detector are set at 15 K for an average FAR of approximately 1%. The last spectrogram of Fig. 10 provides the Level 2 product after application of the cross frequency algorithm to the Level 1 product.

These algorithms flag most of the clearly visible RFI, but there are still some brightness anomalies visible. Additional pulse blanking algorithms can be subsequently applied in post-processing (on an as-needed basis) over a time period of 1 hour at 100 ms time resolution for the integrated power of each channel to help mitigate some of these anomalies. Sub-band kurtosis was also calculated in the real-time data, however, pulsed interference in the time domain caused all frequency bins to appear non-Gaussian in the spectral domain, resulting in all of the data falsely being flagged by the sub-band kurtosis algorithm rather than only removing the pulse. Future campaigns will discard data flagged by Level 1 processing before calculating sub-band kurtosis to remedy this issue. Recalculating sub-band kurtosis in post-processing did not have a significant impact on the data and was not included for these analyses, but it will continue to be studied for this and future data sets.

VI. Field Results

A field campaign for UWBRAD was conducted from September 12-15, 2016. The system was installed on a DC-3 Basler aircraft supplied by Kenn Borek Airlines and was operated on a transit flight from Calgary to Thule Airbase, Greenland and then on a flight from Thule airbase in Greenland. A photo of the flight configuration is presented in Fig. 9.

Fig. 10 shows the path of the transit flight and spectrogram results from Calgary to Cambridge Bay, Canada on September 12th, 2016. Fig. 11 illustrates the campaign flight path and spectrogram results out of Thule on Sept 15th, 2016. Each figure also includes a sample of the time series that includes water and land observations (integrated over the entire 1500 MHz bandwidth of UWBRAD). The region observed in Fig. 11 includes sea scenes, “rock” regions near the coast, as well as portions of the Greenland ice sheet where ablation, wet snow, percolation, and dry snow, respectively, are expected to be dominant processes influencing the thermal emission of the upper portion of the ice sheet. Flights over water scenes were conducted on both flights for external calibration. Estimates of water temperature and salinity are used to derive the expected brightness temperature of the scene. This information is used to determine the losses of the antenna and cable at the input of the radiometer to convert retrieved antenna temperatures into scene brightness. The brightness temperatures in these figures are reported at 244 kHz (125 MHz/512 bins) x 100 ms resolution (Note: The spectrograms in these figures include the band edges of each channel to make the image clearer, but these are removed from the integrated time series. In some cases this appears as a brightness anomaly localized in frequency in the spectrogram).

Fig. 9: Flight configuration of UWBRAD

The time series plots in Fig. 10 and Fig. 11, which are integrated over all available UWBRAD measurements from 500-2000 MHz (discounting band edges), illustrate values obtained prior to any RFI processing (Level 0), after Level 1 processing (Level 1), and after Level 2 processing (Level 2), respectively. The significantly smoother curves resulting after both processing levels appear to correspond to geophysical expectations, although some residual RFI contributions remain in this full spectrum product that are reduced in individual UWBRAD channels.

In Fig. 10, a water crossing of Lake Athabasca can be seen around 8:40-9:00. The times prior to this were over more populated portions of Canada (e.g., Calgary and Edmonton), while times after this were less populated. In the spectrograms, it can be seen that large portions of the spectrum (channels 1-5 and 12, or from roughly 480 – 1230 MHz and above 1920 MHz) are flagged as RFI before reaching the lake, but there is more usable data after the crossing. Most of this is caught by the Level 1 processor, but some of it persists in channels 5 and 12 (840-970 and 1920-2020 MHz range). Looking at the integrated time series (which only plots the data from 8:00-10:00 for clarity), prior to ~9:15, the Level 0 and Level 1 products look drastically different from the Level 2 product, with extremely large positive and negative values (negative values can occur when RFI is strong enough to leak through and impact the reference or noise diode measurements), indicating a very challenging RFI environment. After this time, the Level 1 and Level 2 products have a similar shape but a temperature bias, likely indicating persistent and stable RFI, possibly self-interference from the instrument or aircraft.

In Fig. 11, heavy RFI is visible in the Level 0 product from 12:45 to 13:05, and again after 13:15. The Level 1 processing removes much of this RFI, and the Level 2 processing removes some of the lower power RFI present over the water. Several spikes are still visible over the water, some of which are clearly artificial (ones that exceed the scale of the figure), and others that need further analysis to determine whether they are residual RFI or caused by ice or rock in the scene. Similar to the latter portion of the time series in Fig. 10, there appears to be a bias between the Level 1 and Level 2 products, though it is smaller in magnitude for this flight than in the transit flight. The UWBRAD team is also investigating forward modeling of the full 500-2000 MHz measured data for the differing portions of the Greenland ice sheet observed. A more detailed analysis of this work can be found in Jezek [8].

To illustrate the RFI encountered during these flights, complementary cumulative distribution functions (ccdf's) of the magnitude of RFI encountered in each channel are presented in Fig. 12 (transit flight) and Fig. 13 (Greenland flight). The twelve channels have been distributed among three different graphs for clarity. The x-axis represents the difference in brightness temperature between one RFI mitigation level and the previous level; i.e., a "Level 1" plot indicates the difference in integrated brightness magnitude between the Level 0 raw data and the Level 1 RFI mitigated product, and the "Level 2" plot is the difference between the Level 1 and Level 2 mitigated products. The y-axis shows the percentage of acquisitions where the brightness temperature difference exceeded the RFI magnitude on the x-axis. Level 0 to Level 1 plots are solid lines, and Level 1 to Level 2 are dashed. The analysis presented is meant to illustrate the RFI environment that can be expected when performing radiometry in these unprotected bands rather than a comparison of the individual algorithms' performances. It is divided into two levels to indicate RFI removed in the time domain (Level 1) versus the frequency domain (Level 2), and the results show that significant RFI is removed in each domain and that both levels of processing are beneficial.

The figures show that a wide range of RFI sources were encountered, with magnitudes ranging up to 1 million K. This is not unexpected as no channel was operating in a protected band, so some very strong signals were encountered. Examples of amplifier saturation in the RF unit could also be seen, where a strong interferer in one channel caused a reduction in gain across all channels. For example, between 12:50 and 13:10 in the Level 0 spectrogram of Fig. 11, there are brightness anomalies across all frequency that are removed after Level 1 processing, indicating a pulsed interferer that is present in all channels. In many cases, nearly 100% of the acquisitions for a channel show some level of RFI. This is due to a combination of false alarms in the flagging algorithm and persistent internal RFI sources (particularly for Level 1 to Level 2 processing) that are not separated from external contributions in these analyses.

Comparing all of the channels, it is apparent that RFI below 1 GHz (channels 1 through 4) is generally more frequent and more powerful than at other frequencies. This is evidenced by it staying at higher percentages for higher levels of RFI, as well as reaching higher overall levels of RFI than other channels. RFI in channel 12 (1980 MHz) was prevalent near the population centers in Canada (indicated in the spectrograms of Fig. 10 prior to and over Lake Athabasca), but more in line with the other channels in Greenland and low population areas. The results do not treat saturation effects differently from in-band interferers, so this may skew some of the statistics. Low-level RFI is common in all channels, some of it likely self-interference generated on-board the aircraft (either from the equipment or the aircraft itself).

The UWBRAD flight plan was intended to pass over multiple core sites in the central Greenland ice sheet and end in Sondrestrom, Greenland. Unfortunately, the RF frontend unit experienced two failures in the campaign: one shortly after takeoff from Cambridge Bay on the transit flight to Greenland, and a second failure on the backup unit after ~90 minutes of collecting data in Greenland. Both failures showed damage to the initial amplifiers in the front end chain. It was determined that the damage appeared to be caused by an excessively high input signal. This may have been caused by a buildup and discharge of static electricity in the antenna or a strong signal from one of several high power radars in the area (airports, North Warning System, Ballistic Missile Early Warning System). A bandpass filter, power limiter and ESD diode were added to the input to protect against ESD and strong RFI environments, and a second campaign to achieve observations of the central portion of the Greenland ice sheet was successfully carried out in September 2017 and will be featured in future publications.

Fig. 10: Flight line for transit path data on September 12 (directly right). Level 0 (left top), Level 1 (left middle), and Level 2 (left bottom) brightness spectrograms for entire transit flight. A sample of the integrated time series (over Lake Athabasca) is located directly to the right of each spectrogram.

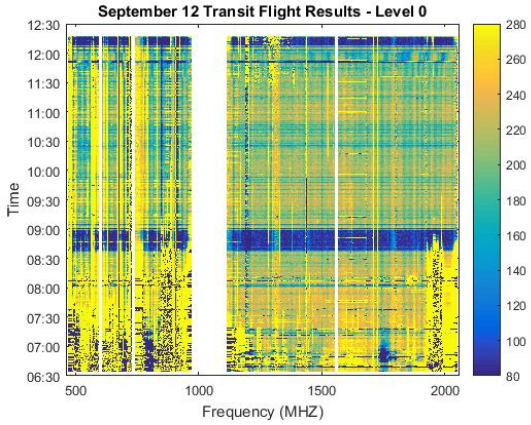

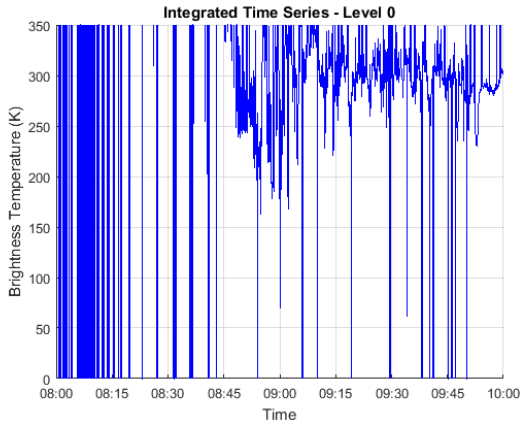

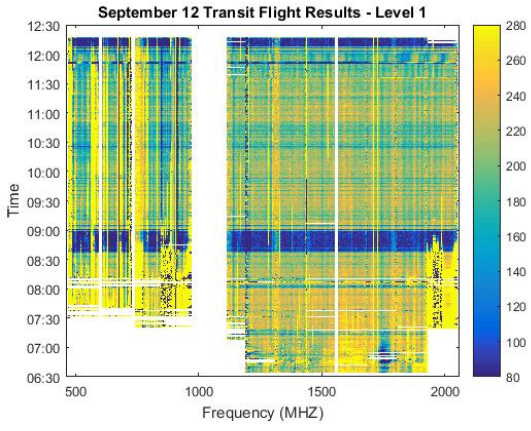

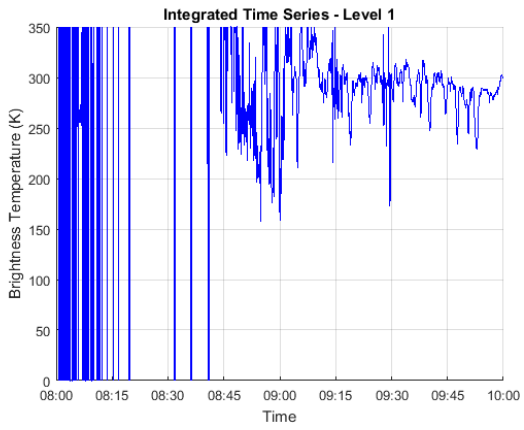

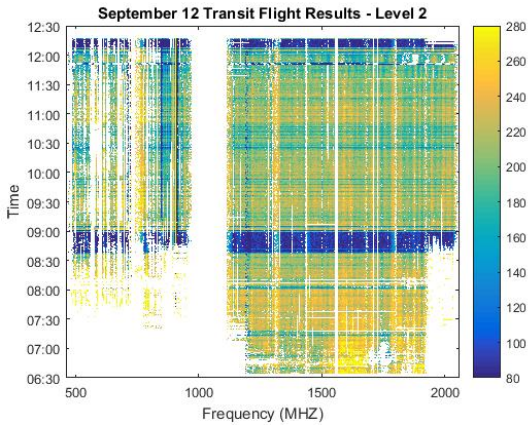

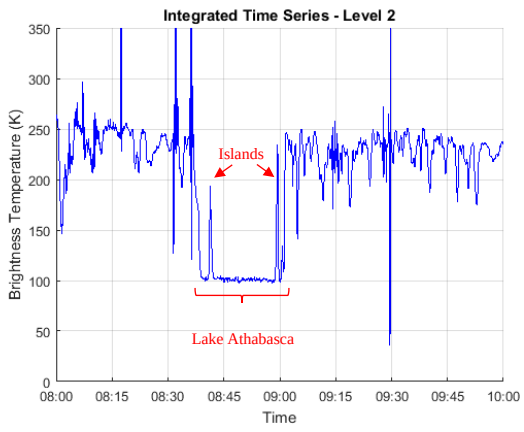

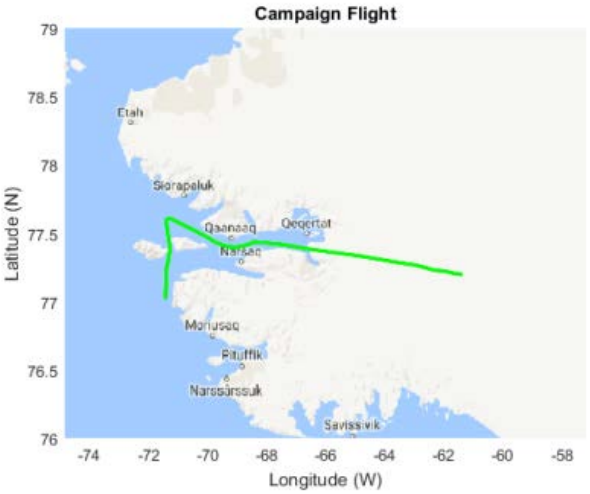

Fig. 11: Flight line for campaign path data on September 15 (directly right). Level 0 (left top), Level 1 (left middle), and Level 2 (left bottom) brightness spectrograms for entire transit flight. The integrated time series is located directly to the right of each spectrogram.

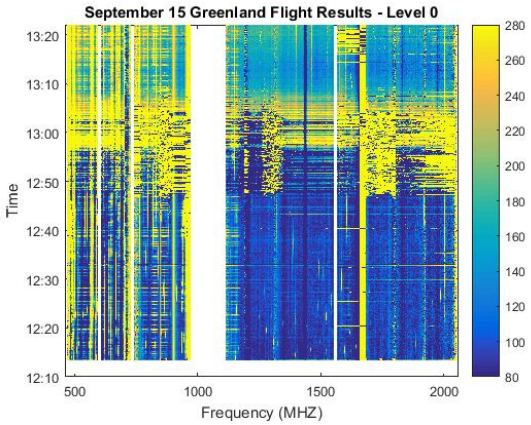

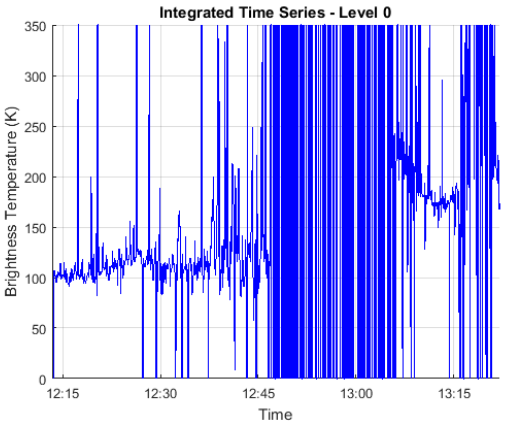

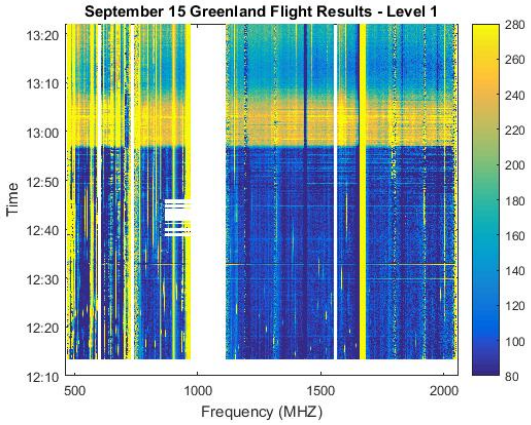

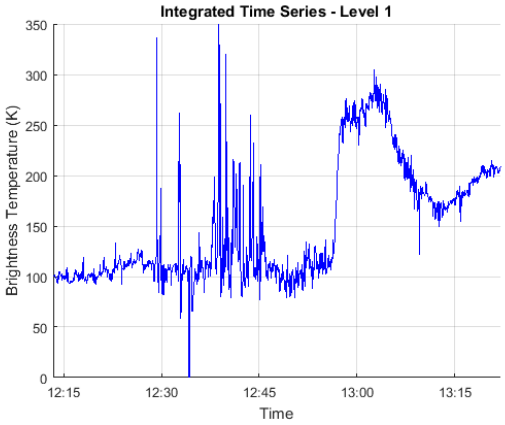

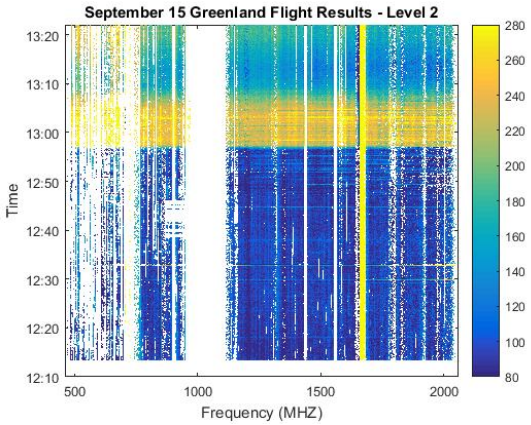

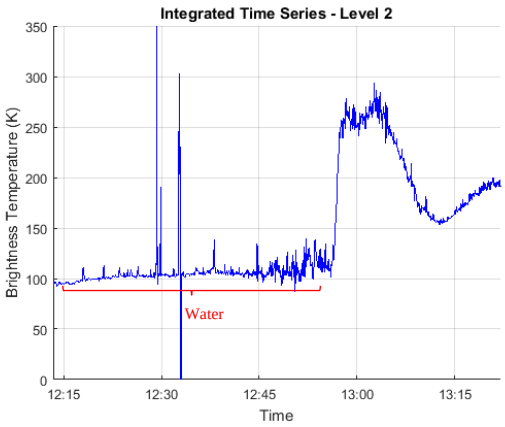

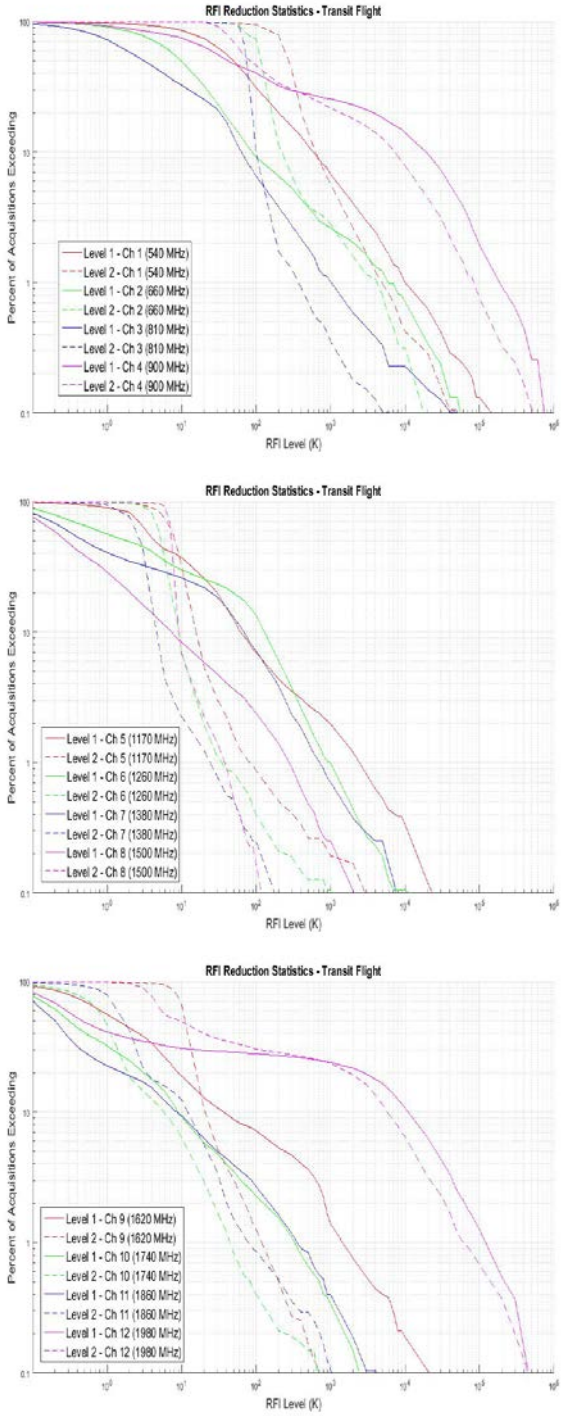

Fig. 12: RFI encountered during transit flight for channels 1 through 4 (top), 4 through 8 (middle), and 9 through 12 (bottom)

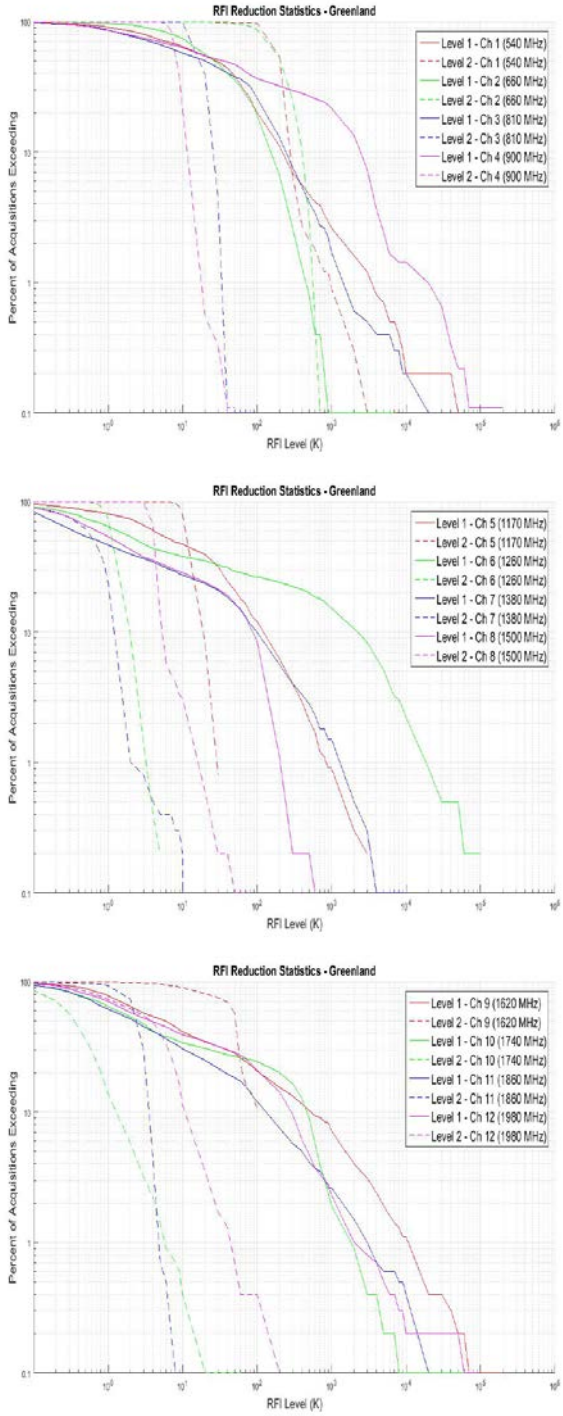

Fig. 13: RFI encountered during Greenland flight for channels 1 through 4 (top), 4 through 8 (middle), and 9 through 12 (bottom)

VII. Conclusion

UWBRAD has shown through lab tests and a field campaign that it is capable of making stable and accurate ultra-wideband radiometric measurements over the 500-2000 MHz frequency range in the presence of significant RFI. It has also provided information regarding the strength and prevalence of signal interference in this unprotected portion of the spectrum. The UWBRAD team is still analyzing the data that the instrument collected from this field campaign, as well as comparing it to data obtained in a second campaign carried out in September 2017. Access to wideband brightness temperatures outside of protected science bands will be invaluable for the future of ice sheet subsurface temperature analysis, and the team is optimistic that UWBRAD will be able to provide this information.

VIII. References

[1] Jezek, K. C., J. T. Johnson, M. R. Drinkwater, G. Macelloni, L. Tsang, M. Aksoy, and M. Durand, "Radiometric approach for estimating relative change in intra-glacier average temperature," *IEEE Trans. Geosc. Rem. Sens.*, vol. 53, iss. 1, pp. 134-143, May 2014.

[2] M. Aksoy, J. T. Johnson, K. C. Jezek, M. Durand, M. R. Drinkwater, G. Macelloni, and L. Tsang, "An examination of multi-frequency microwave radiometry for probing subsurface ice sheet temperatures," Presented at IGARSS, Jul 2014. DOI: 10.1109/IGARSS.2014.6947265.

[3] Brogioni, M., S. Pettinato, F. Montomoli, K. Jezek, and G. Macelloni, "Simulating multi-frequency ground based radiometric measurements at DOME-C Antarctica," *IEEE JSTARS*, vol. 8, iss. 9, pp. 4405-4417, May 2015. DOI: 10.1109/JSTARS.2015.2427512.

[4] Tan, S., M. Aksoy, M. Brogioni, G. Macelloni, M. Durand, K. Jezek, T. Wang, L. Tsang, J. T. Johnson, M. Drinkwater, L. Brucker, "Physical models of layered polar firn brightness temperatures from 0.5-2 GHz," ," *IEEE JSTARS*, vol. 8, iss. 7, pp. 3681-3691, Mar. 2015. DOI: 10.1109/JSTARS.2015.2403286.

[5] Picard, G., Brucker, L., Roy, A., Dupont, F., Fily, M., Royer, A., and Harlow, C.: Simulation of the microwave emission of multi-layered snowpacks using the Dense Media Radiative transfer theory: the DMRT-ML model, *Geosci. Model Dev.*, 6, 1061-1078, https://doi.org/10.5194/gmd-6-1061-2013, 2013.

[6] A. Bringer, et al, "An examination of models for predicting the 0.5-2 GHz brightness temperature of ice sheets," Presented at IGARSS, 2015.

[7] T. Wang, L. Tsang, J. T. Johnson, K. C. Jezek, and S. Tan, "Partially coherent model for the microwave brightness temperature of layered snow firn with density variations and interface roughness," Presented at IGARSS, 2015.

[8] K. Jezek, J. Johnson, S. Tan, L. Tsang, M. Andrews, M. Brogioni, G. Macelloni, M. Durand, C-C. Chen, D. Belgiovane, Y. Duan, C. Yardim, H. Li, A. Bringer, V. Leuski, M. Aksoy, "500-2000 MHz Brightness-Temperature Spectra of the Northwestern Greenland Ice Sheet", accepted by TGRS Nov 2017, DOI: 10.1109/TGRS.2017.2764381.

[9] D. Belgiovane, C. Chen, J. Johnson, "Conical log spiral antenna development for the UWBRAD ice sheet internal temperature sensing". Presented at APSURSI June 2016, DOI: 10.1109/APS.2016.7696619.

[10] J. Piepmeier, J. Johnson, P. Mohammed, et al. "Radio-Frequency Interference Mitigation for the Soil Moisture Active Passive Microwave Radiometer", *IEEE Trans. Geosc. Rem. Sens.*, vol. 52, iss. 1, pp. 761-775, Oct 2013. DOI: 10.1109/TGRS.2013.2281266.

[11] L.W. Peck, D.E. Fenech "SERPent: Automated reduction and RFI-mitigation software for e-MERLIN," *Astronomy and Computing*, Vol. 2, pp.54-66, Aug. 2013. https://doi.org/10.1016/j.ascom.2013.09.001

[12] Guner, B., N. Niamsuwan, and J. T. Johnson, 2007. "Time and frequency blanking for RFI mitigation in microwave radiometry", *IEEE Trans. Geosc. Rem. Sens.*, vol. 45, iss. 11, pp. 3672—3679, Oct 2007. DOI: 10.1109/TGRS.2007.903680.

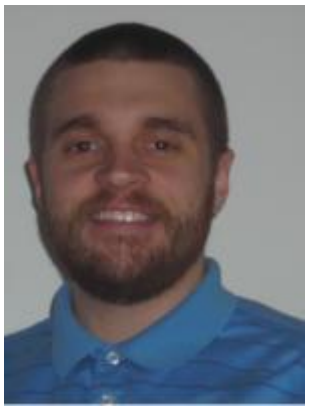

Mark J. Andrews received his B.S. in Electrical and Computer Engineering from Ohio State in 2008. He obtained his M.S in Electrical Engineering from University of Southern California while working as a Payload Systems Engineer for Boeing Satellite Development Center in El Segundo, CA. In August 2013, he returned to Columbus, OH as a Radar Systems Engineer with STAR Dynamics in Hilliard. Beginning March 2014, he has been a Research Associate at the OSU's ElectroScience Laboratory focusing on radar and radiometry research while pursuing his Ph.D.

Joel T. Johnson (S'88-M'96-SM'03-F'08) received the bachelor of electrical engineering degree from the Georgia Institute of Technology in 1991 and the S.M. and Ph.D. degrees from the Massachusetts Institute of Technology in 1993 and 1996, respectively. He is currently Professor and Department Chair in the Department of Electrical and Computer Engineering and ElectroScience Laboratory of The Ohio State University. His research interests are in the areas of microwave remote sensing, propagation, and electromagnetic wave theory. Dr. Johnson is an IEEE Fellow, a member of commissions B and F of the International Union of Radio Science (URSI), and a member of Tau Beta Pi, Eta Kappa Nu, and Phi Kappa Phi. He received the 1993 best paper award from the IEEE Geoscience and Remote Sensing Society, was named an Office of Naval Research Young Investigator, National Science Foundation Career awardee, and PECASE award recipient in 1997, and was recognized by the U. S. National Committee of URSI as a Booker Fellow in 2002.

Kenneth C. Jezek is a Professor Emeritus at the Byrd Polar Research Center, School of Earth Sciences of The Ohio State University (OSU). He received the B.S. degree in Physics from the University of Illinois in 1973 and went on to receive M.S. and Ph.D. degrees in Geophysics from the University of Wisconsin, Madison where he studied the behavior of the Ross Ice Shelf Antarctica using ice sounding radar data collected during several visits to the Antarctic. Before joining OSU's Byrd Polar Research Center as Director in 1989, Dr. Jezek was a geophysicist with the U.S. Army Cold Regions Research and Engineering Laboratory. There, he researched the electromagnetic and acoustical properties of sea ice in the lab and in the Arctic. He also served a two-year term as manager of NASA's polar oceans and ice sheets program. From 1997-2007 he led the Radarasat Antarctic Mapping Project. From 2007 to 2010 he was co-leader of the International Polar Year GIIPSY project which involved the participation of 12 space agencies. He chaired the Land Ice Science Team for NASA's Operation Icebridge from 2010-2013. Since 1989, Dr. Jezek has served on 13 NRC committees. His most recent interests include application of ultra wide-band radiometry to ice sheet and sea ice studies.

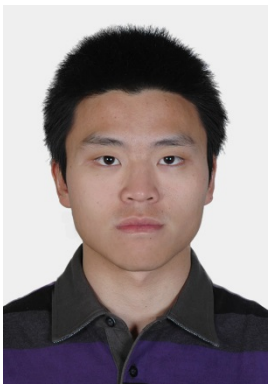

Hongkun Li was born in Guangdong, China, in 1984. He received the B.S. and M.S. degrees in optics from the South China University of Technology, Guangzhou, China, in 2007 and 2010, respectively, and the M.S. degree and the Ph.D. degree in electronics from the University of Nantes, Nantes, France, in 2009 and 2012, respectively. The work in this paper was finished when he was a Post-Doctoral Researcher with the ElectroScience Laboratory, The Ohio State University, United States. His research domain concerns microwave remote sensing, scattering/reflection of microwave/infrared wave from sea-like rough surfaces.

Alexandra Bringer is currently working at the ElectroScience Laboratory, The Ohio State University as a senior research associate. She obtained her M.S and Ph.D. in physics from the Université du Sud-Toulon-Var, La Garde, France, in 2009 and 2012 respectively. Her studies were focused on physical oceanography and remote sensing. Dr. Bringer joined the Electroscience Laboratory for a post-doctoral position in 2014. Since then, she is working on microwave radiometry for cryosphere applications and Radio frequency Interference detection and mitigation. Her main research interests are microwave remote sensing, ocean and cryosphere remote sensing and signal processing.

Chi-Chih Chen (S'92–M'97–SM'07-F'15) received his MS and Ph.D. degrees from the Ohio State University Electrical and Computer Engineering Department in 1993 and 1997, respectively. He has been with The Ohio State University ElectroScience Laboratory since 1993 and became a Postdoctoral Researcher in 1993, Senior Research Associate in 1999, Research Scientist in 2004, Research Associate Professor at OSU Electrical and Computer Engineering Department in 2011. He is also the Chief Technology Officer of Nikola Labs since 2017. Dr. Chen received Lumley Research Awards (2004, 2010, 2015), Inventors Award (2016), Lumley Interdisciplinary Award (2016), and Inventors Award (2016) from OSU College of Engineering. He also received Distinguished Achievement Award from Antenna Measurement Techniques Association in 2016. Dr. Chen's research area includes ground penetrating radars (GPR), automobile radars, UWB antennas and arrays, small antennas, GPS/GNSS antennas, wearable antennas, wireless energy harvesting and delivery, and sensor networks. He served as Treasurer, Vice Chairman and Chairman of IEEE Joint AP/MTT Columbus Chapter (2001-2003). He served as Technical Coordinator, President, and Past President of AMTA (2012-2015). He has served on Technical Program Committees of IEEE APS/URSI Symposiums, PAST Symposiums, IGARSS Symposiums, and European Conference on Antennas and Propagation (EuCAP). He was the Technical Chair of 2006 International GPR Conference for which he has been a member of the International Advisory and Science Committee since. Dr. Chen is a Fellow of IEEE and a Fellow of AMTA; Member of Exploration Geophysicists Society (SEG), Sigma Xi, and Phi-Kappa-Phi.

Domenic J. Belgiovane, Jr. (S'2012) received his MS and BS Degrees in Electrical and Computer Engineering from The Ohio State University, in 2013 and 2017, respectively. In the past he has worked at companies such NASA's Glenn Research Center, Honda of America Manufacturing, ViaSat Inc., and Space Exploration Technologies. Currently, he is pursuing his Ph.D. at The Ohio State University's ElectroScience Laboratory, expected to graduate in the December of 2017. Domenic's research interests include vehicular obstacle detection, millimeter radar cross section measurement, automotive radar propagation environments and target modeling, surrogate target development for automatic emergency breaking protocols, novel radar systems, and antenna designs.

Giovanni Macelloni (M'07) received the M.Sc. degree in electronic engineering from the University of Florence, Florence, Italy, in 1993. Since 1995 he works at Institute of Applied Physics-CNR-Florence where is now senior scientist. In the last 15 years his main research interest concerns the investigation on snow and the cryosphere, in particular in the polar regions, by means of active and passive microwave remote sensing. It is the leader of the IFAC research unit, in national (PNRA) and international projects (ESA, EC) related to the cryospheric science and he organized several scientific campaigns in Antarctica. He was a member of the Mission Advisory Group of the ESA's COREH20 (Cold Regions Hydrology High-Resolution Observatory) mission during Phase-0 and Phase-A and he is currently involved in the team which propose new spaceborne missions for investigating on terrestrial snow. He is a member of the Cryonet team of Global Cryosphere Watch of the WMO, of the Italian Scientific Antarctic Commission, of the committee of EC-COST action on Snow Hydrology. It served as reviewer of several international committees and organizations and international journals, participated in the organization of several international conferences and was co-chair of international conferences.

Marco Brogioni was born in Siena, Italy, in 1976. Since 2004, he has been with the Istituto di Fisica Applicata "N. Carrara" - IFAC, Consiglio Nazionale delle Ricerche, Sesto Fiorentino, Italy, working in the Microwave Remote Sensing Group. He get the MSc in Telecommunications Engineering at the University of Siena, Italy, in 2003 and the PhD in Remote Sensing at the University of Pisa, Italy, in 2008. In 2006 and 2007 he has been visitor student at the University of California, Santa Barbara, CA. His research deals mainly with passive and active microwave remote sensing applied to snow by using satellite and ground-based data. In particular, the development of electromagnetic models for passive and active microwave remote sensing of snow, vegetation and soil. He is also involved in the design and manufacturing microwave radiometers (L- to Ka-band). In 2008 he was in the local organizing committee of the 10th Microrad symposium held in Florence, Italy and in 2010 he was in the local organizing committee of the 2010 Microwave Signature Symposium of the URSI Commission-F still held in Florence. In 2008 he was awarded with the third prize at the URSI GA Student Prize Paper Competition in Chicago, IL. In 2013 and 2015 he participated to the Italian Antarctic Expeditions carrying out his research at Concordia Station (Dome-C). At present is involved in several projects regarding polar regions.